

**Role of graphite crystal structure on the shock-induced formation of cubic and hexagonal diamond**Travis J. Volz<sup>1,2</sup>, Stefan J. Turneaure<sup>2</sup>, Surinder M. Sharma<sup>2</sup> and Y. M. Gupta<sup>1,2,\*</sup><sup>1</sup>*Department of Physics and Astronomy, Washington State University, Pullman, Washington 99164, USA*<sup>2</sup>*Institute for Shock Physics, Washington State University, Pullman, Washington 99164, USA*

(Received 2 March 2020; revised manuscript received 5 May 2020; accepted 7 May 2020; published 9 June 2020)

Since cubic diamond was first recovered from explosively shocked graphite samples in 1961, the shock-induced graphite to diamond phase transformation has been of great scientific and technological interest. Recent real-time x-ray diffraction results on different types of pyrolytic graphite under shock compression have reported hexagonal diamond and cubic diamond formation at comparable stresses. To resolve and understand these differences, synchrotron x-ray diffraction measurements were used to examine, in real time, the plate impact shock response of two grades of highly oriented pyrolytic graphite and as-deposited pyrolytic graphite—at stresses below and above their respective phase transformation stresses. The present results show that at their respective transformation stresses, crystallites in as-deposited pyrolytic graphite are compressed  $\sim 30\%$  more along the  $c$  axis than crystallites in both highly oriented pyrolytic graphite types. This work establishes that the high-pressure phase of even ZYH-grade highly oriented pyrolytic graphite (a less oriented variety with mosaic spread  $3.5^\circ \pm 1.5^\circ$ ), at  $\sim 50$  GPa, is hexagonal diamond. In contrast, the high-pressure phase of as-deposited pyrolytic graphite (mosaic spread  $\sim 45^\circ$ ) in the present work, at  $\sim 60$  GPa, is cubic diamond. Analysis of ambient x-ray diffraction data demonstrates that the crystallites in the highly oriented pyrolytic graphite samples have the hexagonal graphite crystal structure with three-dimensional long-range order. In contrast, the crystallites in the as-deposited pyrolytic graphite samples have a turbostratic carbon crystal structure which lacks rotational/translational order between parallel adjacent graphene layers. The ambient results suggest that the observed high-pressure crystal structure of shocked graphite depends strongly on the initial crystal structure—shock compression along the  $c$  axis of hexagonal graphite (in highly oriented pyrolytic graphite) results in highly textured hexagonal diamond and shock compression of turbostratic carbon (in as-deposited pyrolytic graphite) results in nanograined cubic diamond. The present results reconcile previous disparate findings, establish the definitive role of the initial crystal structure, and provide a benchmark for theoretical simulations.

DOI: [10.1103/PhysRevB.101.224109](https://doi.org/10.1103/PhysRevB.101.224109)**I. INTRODUCTION**

Transformation of graphite into diamond under extreme thermodynamic conditions has fascinated researchers for more than six decades [1–8]. This phase transformation displays contrasting features of being very slow (minutes) under static compression [9,10] and extremely rapid (nanoseconds) under shock compression [4,7].

Under static compression, experimental [2,5,11,12] and theoretical [13–15] studies of the graphite to diamond transformation have provided useful insights. Early studies showed that pyrolytic graphite and amorphous carbon [2], as well as rhombohedral graphite [13,14], transformed to the cubic diamond crystal structure, while highly ordered hexagonal graphite can transform to the hexagonal diamond crystal structure [5,11,12,15]. The latter diamond form, also known as Lonsdaleite [3], is believed to be a harder carbon polymorph than cubic diamond [16,17]. However, other studies have revealed that for a large variety of initial graphites, the terminal phase depends on the thermodynamic

path experienced, resulting in a varying abundance of coexisting cubic and hexagonal phases [8–10]. Recent studies [18–20], which reanalyzed previously recovered hexagonal diamond samples or XRD patterns from samples previously suggested to contain hexagonal diamond, have reported that the earlier structures were not pure hexagonal diamond and may more accurately be described as stacking disordered cubic diamond. Several other studies also claim the existence of many lower-symmetry  $sp^3$  bonded carbon crystal structures [21–26]. Although static compression and recovery experiments provide some insights into the graphite to diamond transformation, the vastly different timescales in those experiments limit their utility for a detailed understanding of the transformations occurring in shock-compressed graphites—the focus of this work.

The first observation of diamond recovered after explosive shock compression of graphite was in 1961 [1]. This work motivated the correlation of subsequent observations of diamond in meteoritic craters to the impacts of meteorites with earth [27] or their parent bodies in space [28,29]. These studies also provided justification for the use of meteorite impact diamonds as markers of natural cataclysmic impact events [30].

\*ymgupta@wsu.edu

Despite finding diamond in remnants of shocked graphites [1] and meteorites [27,29], real-time evidence for the likely occurrence of this structural change within several nanoseconds was not reported until the 1990s [4,31]. In these plate impact shock experiments, wave profile measurements on highly oriented pyrolytic graphite samples were analyzed to infer nanosecond transformations (only for ZYB-grade samples with  $\sim 0.8^\circ$  mosaic spread of the graphite  $c$  axis from the sample normal) to a phase with diamondlike density [4,31]. Very recent wave profile measurements in plate impact experiments have also established nanosecond transformation times for less orientationally ordered graphite types [7]: ZYH-grade highly oriented pyrolytic graphite ( $c$ -axis mosaic spread  $\sim 3.5^\circ$ ) and as-deposited pyrolytic graphite ( $c$ -axis mosaic spread  $\sim 40^\circ - 50^\circ$ ). However, the shock stress required to initiate the phase transformation in the as-deposited pyrolytic graphite was twice as large as for both highly oriented pyrolytic graphite types [7]. This finding shows the strong dependence of the phase transformation on the starting graphite material. Although these wave profile (or continuum) measurements [4,7,31] are valuable in providing the stress-density states under shock compression, they do not provide the crystal structure of the high-pressure phase.

Direct observations of the crystal structure on nanosecond timescales in shock-compressed graphite have been achieved only recently—through real-time *in situ* x-ray diffraction (XRD) measurements [32,33]. The results of these two studies are contradictory, as are related computational studies under rapid compression conditions [34–37]. The laser-shock XRD study [32] reported transformation of pyrolytic graphite to cubic diamond at  $\sim 55$  GPa and to hexagonal diamond above  $\sim 170$  GPa. In contrast, XRD measurements in plate impact shock experiments on ZYB-grade highly oriented pyrolytic graphite demonstrated an unambiguous transformation to a highly textured hexagonal diamond structure at 50 GPa shock stress [33].

Understanding the contrasting real-time results from these two XRD experimental studies [32,33]—using different shock compression approaches—and determining the key factor(s) governing the crystal structures of the high-pressure phases formed during shock compression of graphite are the primary motivations of the present work. Toward this end, careful *in situ* XRD measurements were performed during plate impact shock compression experiments on three graphite types (ZYB-grade and ZYH-grade highly oriented pyrolytic graphite, and as-deposited pyrolytic graphite). All graphite types were studied below their respective phase transformation stresses to gain a detailed understanding of the shock-compressed states prior to the transformation, and ZYH-grade highly oriented pyrolytic graphite and as-deposited pyrolytic graphite were studied above their respective transformation stresses. We note that the shock response of ZYH-grade highly oriented pyrolytic graphite, having an intermediate degree of orientational order between as-deposited pyrolytic and ZYB-grade highly oriented pyrolytic graphite, has not been previously examined using *in situ* XRD measurements. Plate impact loading was used in all experiments to eliminate possible differences due to different shock loading drivers and to provide a direct comparison with the earlier XRD study on ZYB-grade highly oriented pyrolytic graphite [33].

In contrast to the previous *in situ* XRD measurement studies on shock-compressed graphites [32,33], the ambient crystal structures and the ambient microstructures of the various forms of starting graphite materials were carefully characterized. Throughout the text, the following terminology is used to refer to the internal state of a sample: “crystal structure” and “microstructure.” “Crystal structure” or “crystallite structure” is used to refer to the periodic arrangement of the atoms within each crystallite. “Microstructure” is used to refer to the size, alignment, or texture of the crystallites within a bulk sample.

The following specific questions are addressed in this work: (1) Do plate impact experiments on as-deposited pyrolytic graphite result in the formation of cubic diamond or hexagonal diamond? (2) What is the high-pressure phase of the ZYH-grade highly oriented pyrolytic graphite (orientational order intermediate to ZYB-grade highly oriented pyrolytic graphite and as-deposited pyrolytic graphite)? (3) What are the lattice-level structural responses of highly oriented pyrolytic graphite and as-deposited pyrolytic graphite below their respective phase transformation stresses? (4) Can a detailed understanding of the ambient crystallite structures of highly oriented pyrolytic graphite and as-deposited pyrolytic graphite provide insight into the different high-pressure phases [32,33] and continuum [7] responses previously reported under shock compression for the different graphite types?

This paper is organized as follows. Experimental methods are presented in Sec. II. Particular emphasis is given to describing the microstructural characterization of the three graphite types examined. Experimental results are presented in Sec. III. Analysis of the XRD results is presented in Sec. IV. Comparisons of the present results with previous *in situ* XRD results [32,33] are also made in Sec. IV to provide insight into the factors governing the high-pressure phases formed during the shock compression of graphite. Key findings are summarized in Sec. V.

## II. EXPERIMENTAL METHODS

### A. Experimental configuration

A schematic view of the configuration used for the *in situ* x-ray diffraction measurements in shock-compressed graphite is shown in Fig. 1; the overall approach is similar to that presented in Ref. [33]. Using a two-stage light gas gun or a powder gun, a polycarbonate or [100] oriented lithium fluoride (LiF) impactor was launched onto a  $\sim 2$ -mm-thick graphite sample, from the right in Fig. 1. Upon impact, a leftward traveling shock wave(s), with peak longitudinal stress between 9 and 61 GPa, propagates into the graphite sample along the average  $c$  axis, while a rightward traveling shock wave travels into the impactor material. Four XRD frames (153.4 ns apart) were obtained during each impact experiment to characterize the crystal structures of either the compressed graphite or the high-pressure phases, depending on the peak stress achieved. During each frame, the x rays probe multiple materials. As shown in Fig. 1, all materials along the x-ray beam path are probed after impact. Velocity interferometry probes (velocity interferometry system for any

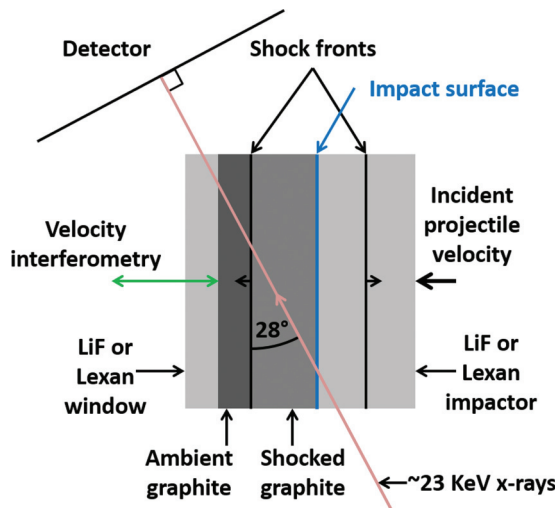


FIG. 1. Experimental configuration for *in situ* plate impact XRD experiments. The snapshot shown is after the flyer plate impacts the graphite sample. Boundaries between shocked and unshocked materials are indicated with black lines and the graphite/impactor interface is indicated with a blue line. The x-ray detector is perpendicular to the direct x-ray beam.

reflector (VISAR) [38,39] and photon Doppler velocimetry (PDV) [40]) were used to obtain wave profiles and shock breakout timing information from the sample rear surface. The shock breakout times were used to correlate the shock event with the time corresponding to each XRD measurement. Frame times relative to impact and other experimental details are reported in the Supplemental Material (SM) [41]; also see Refs. [42–47].

## B. Materials

### 1. Samples, characterization, and preparation

Experiments were performed on ZYB and ZYH-grade highly oriented pyrolytic graphite (HOPG) and on as-deposited pyrolytic graphite (PG). All samples in this study were obtained from Momentive Performance Materials (Strongsville, OH). Sample densities were determined using the Archimedeian method in most experiments and in a few cases, from mass and volume measurements. The ZYB-grade HOPG, ZYH-grade HOPG, and PG had average measured densities of 2.26, 2.25, and 2.21 g/cm<sup>3</sup>, respectively. Sound speeds were measured using the pulse-echo technique [47] for the PG samples and average longitudinal and shear sound speeds were  $3.42 \pm 0.03$  and  $0.83 \pm 0.01$  km/s, respectively. Reliable sound speed measurements were not obtained for the HOPG samples due to large acoustic attenuation [48], a problem previously noted [7,49]. Prior to assembling each target, layers from either side of each HOPG sample were cleaved with Scotch tape to obtain a clean surface for bonding. The PG samples were lightly polished with ÅngströmLap optical polishing paper to decrease the surface roughness to around 1 micron from the ~15-micron roughness resulting from the manufacturing process.

For experiments utilizing a window, each window was characterized prior to the target assembly. The density

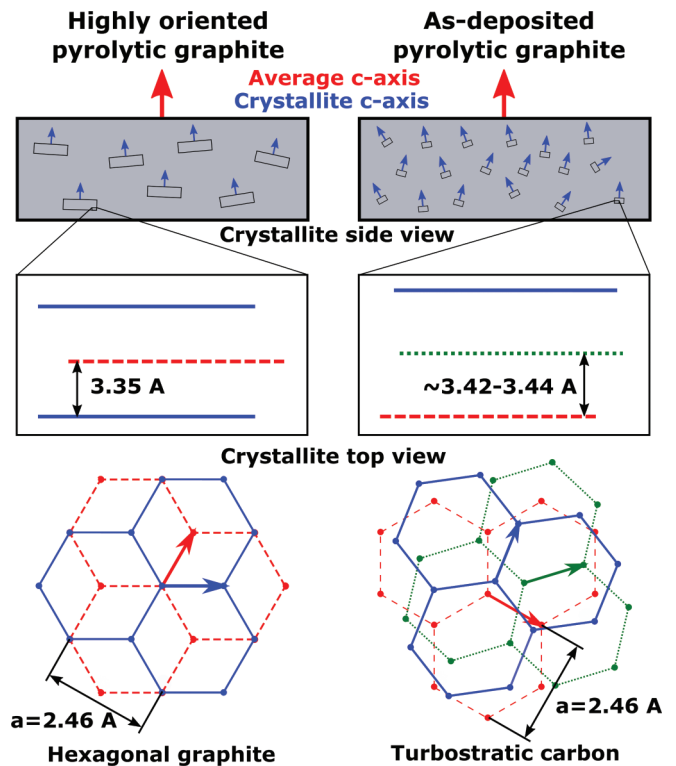


FIG. 2. Comparison of graphite crystal structures and microstructures. HOPG (left) and PG (right) are depicted from the macroscopic scale (top) down to the atomic scale (bottom). The many crystallites comprising the bulk sample are shown with the resulting mosaic spread in the top of the figure. Closeup side views of the crystal structure interlayer spacings are shown in the middle. Top views of the hexagonal graphite and turbostratic carbon crystal structures looking down at the average  $c$  axes are shown at the bottom. Note that the orientations of crystallites transverse to the average  $c$  axis are randomly distributed giving rise to a fiber texture.

of each polycarbonate window was determined using the Archimedeian method while the density of each LiF [100] window was determined geometrically using the measured mass and calculated volume. Average densities for the polycarbonate and LiF windows were 1.19 and 2.63 g/cm<sup>3</sup>, respectively. The longitudinal sound speeds for the polycarbonate and LiF windows were determined using the pulse-echo technique [47]; the average values were 2.28 and 6.62 km/s, respectively.

### 2. Graphite crystal structures and microstructures

A microscopic feature common to all three graphite types examined is a layered structure with strong  $sp^2$  hybridization bonding within the graphene layers and weak bonding along the  $c$  axis normal to the layers. Various forms of graphite differ in the degree and nature of the ordering of the graphene layers (crystallinity) and in the orientation distribution of the crystallite  $c$  axes (mosaic spread). Figure 2 shows schematic diagrams depicting typical HOPG and PG crystallite orientations and crystal structures. As shown at the top of Fig. 2, each bulk sample comprises many crystallites. Although the crystallites have a preferred orientation with the average  $c$  axis aligned perpendicular to the sample face, the basal planes of the



tion spots for hexagonal graphite are observed in the HOPG ambient diffraction patterns [Figs. 3(a) and 3(e)] recorded just prior to the shock compression experiments confirming that the HOPG crystallites are predominantly hexagonal graphite.

In summary, the careful characterization of the ambient samples demonstrates that the various graphite samples differ in two distinct ways: (1) mosaic spread (or orientation distribution) of the crystallite  $c$  axes, and (2) the local crystal structure (either hexagonal graphite with 3D long-range order or turbostratic carbon with 2D order within planes).

### C. X-ray diffraction measurements

The XRD experiments were performed at the Dynamic Compression Sector (DCS) located at the Advanced Photon Source (APS), Argonne National Laboratory. The experiments were performed during the 24-bunch mode which provides  $\sim 100$ -ps duration x-ray pulses every 153.4 ns. The x-ray flux was peaked near 23 keV and was generated from either the first harmonic of a 1.72-cm period insertion device or the third harmonic of a 2.7-cm period insertion device. Two sets of horizontal and vertical Kirkpatrick-Baez (KB) mirrors were used to focus  $\sim 23$ -keV x rays onto the target. The KB mirrors filtered out higher harmonics and thin Al and/or Ag plates filtered out lower harmonics when using the 2.7-cm period undulator. Experimental parameters relating to the x-ray generation and focusing are reported in Table S2 and flux spectra are shown in Fig. S2 for all experimental runs (see Supplemental Material [41]).

During each experiment, four x-ray diffraction (XRD) images were obtained using the DCS custom four-frame x-ray detector system. A cerium-doped lutetium oxyorthosilicate (LSO) x-ray phosphor [57] converts the diffracted x rays from each pulse to visible photons which are then coupled to the four-camera detector array using either a 150- or 75-mm-diameter fiber taper. Three 50:50 beam splitters are used to split the incident light to four separate PI-MAX4:2048f intensified charge-coupled devices (ICCDs) gated to capture diffraction images from individual x-ray pulses creating a four-frame movie of the shock event. During most experiments, at least one image was obtained prior to impact, and several were obtained after impact.

In each experiment, obtaining an image of only the shocked material is unlikely because the projectile impact cannot be completely synchronized with the x-ray bunches from the synchrotron. However, velocity interferometry signals of the shock breakout recorded during the experiment are used to correlate the time of each XRD frame relative to impact. This information allows a determination of the amount and position of the shocked and the ambient material at the time each XRD image was obtained.

For all experiments, the x-ray beam was somewhat offset from the sample center as depicted in Fig. 1 (beam offsets are listed in Table S1) [41]. Offsetting the x-ray beam maximizes the time that x rays probe a sample region under uniaxial strain, since the beam effectively sweeps toward the sample center, initially, after impact. In each experiment, at least one XRD measurement was made on material under purely

uniaxial strain prior to stress release waves from the sample edges reaching the volume probed by x rays.

### D. Continuum measurements

Velocity interferometry measurements were used to record the shock arrival time and particle velocity history at the rear surface of the graphite samples. Both a VISAR [38,39] and a PDV [40] system were used. A VISAR probe was located at the center of each sample and PDV probes were placed at several locations around the center of the sample, as well as at the center of the sample in some experiments using a dual VISAR/PDV center probe. Both VISAR and PDV measurements were made at an aluminum mirror at the rear surface of the graphite sample. For experiments using a window, the aluminum mirror was vapor deposited onto the window which was epoxy bonded to the back of the graphite sample. For experiments without a window, the aluminum coating was deposited directly onto the graphite sample rear surface. A representative velocity history is shown in Fig. S1 [41]. Although wave profiles were obtained in these experiments, shock speeds were not measured. Thus, the in-material states could not be directly determined using the wave profiles. Instead, since the same graphite types were studied in past continuum experiments [7], the previously established Hugoniot were used to determine the in-material states achieved during the XRD experiments through impedance matching with the impactor material as described in the SM [41].

## III. EXPERIMENTAL RESULTS

A total of eighteen *in situ* XRD plate impact experiments were performed in this work: four each on ZYB-grade HOPG, ZYH-grade HOPG, and as-deposited PG below their respective phase transformation stresses; two on ZYH-grade HOPG at  $\sim 50$  GPa, above the phase transformation stress; and four on PG at  $\sim 60$  GPa, above the phase transformation stress. Representative XRD images obtained before the experiment (top row) and after shock waves have entered the sample (bottom row) are shown in Fig. 3. The experiment number, time of each frame relative to impact, and predominant crystal structure are shown for each frame. Due to the many crystallites in the graphite samples and the resulting fiber texture, all diffraction patterns are symmetric about the horizontal center line of each image. Because of the different mosaic spreads characterizing the starting materials (top row of images), the azimuthal peak widths are also different for the different sample types. In addition, due to the much larger mosaic spread of PG samples, diffraction from the  $(00l)$  peaks is also visible in Figs. 3(c) and 3(e) whereas these diffraction peaks are not allowed for the HOPG grades due to the restricted orientation distribution of the crystallite  $c$  axes.

Additional differences in the XRD patterns for the different graphite types arise from the different crystal structures in the samples. As discussed in Sec. II B, only  $(hk)$  and  $(00l)$  peaks are observed for the ambient PG due to the predominantly turbostratic carbon crystallite structure, whereas many general 3D  $(hkl)$  XRD peaks are visible for the HOPG due to the more ordered hexagonal graphite crystallite structure.

### A. Diffraction results below phase transformation stresses

Figures 3(b) and 3(d) show diffraction from both the ambient and shocked material for experiments conducted below the phase transition onset stresses of HOPG and PG, respectively. For the HOPG experiments, many small displacements of the diffraction spots are noticeable; larger shifts are observed for ( $hkl$ ) peaks with larger  $l$  values, as shown for the (100) and (103) peaks, in Fig. 3(b). For PG, the shift of the (002) peak is the only prominent diffraction peak shift. These observations are consistent with greater compression along the  $c$  axis than within graphene layers, a finding quantitatively established later in Sec. IV.

### B. Diffraction results above phase transformation stresses

Figures 3(f) and 3(h) show diffraction images from only the shocked material for experiments conducted above the phase transformation stresses of ZYH-grade HOPG and PG, respectively. A fraction of the corresponding ambient diffraction images was subtracted from the shocked diffraction images to isolate the XRD pattern due to the shock-compressed material. Many new diffraction peaks are apparent for the shock-compressed ZYH-grade HOPG shown in Fig. 3(f), several of which overlap the ambient (100) and (110) peak locations. The observation of many new peaks indicates that a new crystal structure has been formed. For the PG experiments, the (002) and (004) peaks are no longer noticeable after shock compression also indicating a phase change. Significant intensity remains at the location of the ambient (10) turbostratic carbon diffraction peaks and an additional dim peak also appears between the ambient (002) and (004) side peak locations.

## IV. ANALYSIS AND DISCUSSION

### A. X-ray diffraction analysis methods

To ascertain the phases and lattice parameters from the diffraction images recorded for shock-compressed HOPG and PG, a forward x-ray diffraction simulation fitting routine was used. Prior to each experiment, diffraction from a polycrystalline silicon calibration target was used to determine the direct beam location on the detector and to establish the ambient sample to detector distance. A continuum shock wave analysis, described in the SM, was used to determine the effective peak state shocked material thicknesses and sample to detector distances  $D$  at the time each diffraction image was recorded, as reported in Table S1 [41].

#### Determination of lattice parameters

The XRD peak fitting, depicted in Fig. 4 for the peak marked with an asterisk in Fig. 3(a), was carried out as follows. First, each localized XRD peak was integrated azimuthally over a small angular range using the FIT2D CAKE function [41,58] resulting in a line profile (Fig. 4, black line). A background line profile (Fig. 4, green dot-dashed line) was then subtracted resulting in a background subtracted line profile (Fig. 4, blue line). To determine the lattice spacing which best fits each peak, forward diffraction simulations were performed and compared to the background subtracted

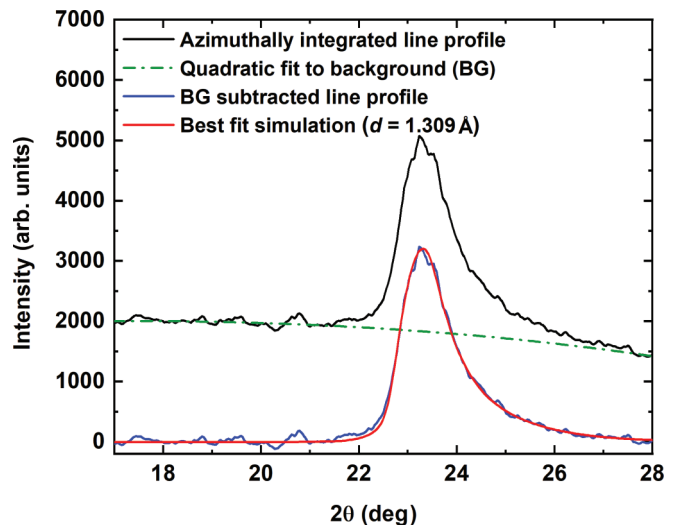


FIG. 4. Representative XRD line profile and fit for a single XRD peak. The azimuthally integrated intensity vs scattering angle line profile (black) is shown along with the background line profile (dot-dashed green) and the resulting background subtracted line profile (blue) is shown below. The best fit simulated XRD line profile is shown in red. The measured and simulated line profiles correspond to the hexagonal graphite (104) peak indicated with an asterisk in Fig. 3(a).

integrated line profiles. The diffraction simulations, based on Bragg's law, utilized the experimental flux spectra taken during each experimental run (see Fig. S2) [41]. The beam size, sample thickness, sample to detector distance for the shocked material, x-ray attenuation through each material present, and Lorentzian instrumental broadening based on the broadening needed to match the diffraction patterns from the silicon calibration target were also used in the simulations. Additional broadening due to crystallite size effects was also implemented for some experiments.

By simultaneously varying the lattice spacing, and in some cases the assumed crystallite size (to determine size broadening) [59], a least-squares fit was used to establish the lattice spacing (and crystallite size) necessary to best match the experimental XRD line profile. The best fit simulated XRD line profile for the representative XRD peak is shown as a red line in Fig. 4. To determine the lattice parameters reported in Table I for the different shocked state crystal structures, the best fit  $d$  spacings for different sets of ( $hkl$ ) peaks were used for different experiments, because the crystal structures and  $hkl$  indices of the available peaks were different below and above the phase transformation stress for each material. The specific ( $hkl$ ) peaks used to determine the lattice parameters for each experiment are discussed in the SM along with additional XRD analysis details [41].

### B. Results of x-ray diffraction analysis

Throughout the following discussion of the results, it is worth noting that the high-pressure states achieved under shock compression are likely somewhat heterogeneous due to the many small crystallites exhibiting a range of orientations. As a result, a range of local stresses near grain boundaries

TABLE I. Experimental results. The high-pressure phases and lattice parameters ( $a$  and  $c$ ) are reported for each experiment, with the experiment numbers shown corresponding to those in Fig. 3. The graphite sample types and peak stresses achieved are also reported for all experiments.

Experiment number	Stress (GPa)	Sample material	Shocked phase	$a$ (Å)	$c$ (Å)
1	14.1	ZYB HOPG	Hex. graphite	$2.446 \pm 0.017$	$5.668 \pm 0.098$
2	14.6	ZYB HOPG	Hex. graphite	$2.441 \pm 0.013$	$5.706 \pm 0.128$
3	17.2	ZYB HOPG	Hex. graphite	$2.441 \pm 0.014$	$5.665 \pm 0.095$
4	20.5	ZYB HOPG	Hex. graphite	$2.444 \pm 0.009$	$5.561 \pm 0.094$
5	9.5	ZYH HOPG	Hex. graphite	$2.453 \pm 0.018$	$5.940 \pm 0.106$
6	16.0	ZYH HOPG	Hex. graphite	$2.447 \pm 0.007$	$5.670 \pm 0.085$
7	17.3	ZYH HOPG	Hex. graphite	$2.444 \pm 0.008$	$5.637 \pm 0.057$
8	20.7	ZYH HOPG	Hex. graphite	$2.436 \pm 0.016$	$5.553 \pm 0.125$
9	14.9	PG	Turbo. carbon	–	$5.773 \pm 0.041$
10	29.9	PG	Turbo. carbon	–	$5.454 \pm 0.041^a$
11	38.7	PG	Turbo. carbon	–	$5.312 \pm 0.022$
12	46.8	PG	Turbo. carbon	–	$5.247 \pm 0.021$
13, 14	49.0 avg.	ZYH HOPG	Hex. diamond	$2.473 \pm 0.027$	$4.154 \pm 0.017$
15–18	59.5 avg.	PG	Cub. diamond	$3.549 \pm 0.017$	–

<sup>a</sup>Only one diffraction peak was used to determine  $c$ , so the uncertainty was based on the uncertainties in peak position and detector distance through the sum of squares uncertainty propagation formula.

and in different individual crystallites likely exists. Since the crystallites ( $\sim 0.01\text{--}1\ \mu\text{m}$ ) are much smaller than the probe beam ( $\sim 800\ \mu\text{m}$ ), the observed diffraction patterns represent an average response over many crystallites.

### 1. Lattice parameters below phase transformation stresses

For experiments below the transformation stress of each graphite type, compression mainly occurred along the  $c$  axis of the graphite crystallites. For all graphite types, minimal  $a$ -axis compression was observed as consistent with the stronger in-plane bonding relative to the bonding between layers, as evidenced by the much larger in-plane elastic constants [48]. A similar finding was reported previously [60]. The limited  $a$ -axis compression is apparent from the lack of an obvious shift of the (10) PG and (100) HOPG diffraction peaks. The lattice parameters for shocked graphite below the transformation stress are listed in Table I and the relative  $c$ -lattice parameters ( $c/c_0$ ) for all experiments below the transformation stresses are shown in Fig. 5. The relative  $c$ -axis lattice parameters follow a similar curve for all graphite types, but the following observations are noteworthy. The lattice parameters determined for both HOPG grades were consistent below the phase transformation stress and exhibited a  $\sim 17.5\%$   $c$ -axis compression at the 22-GPa transformation stress. In contrast, for PG, while the  $a$ -axis lattice parameters could not be directly established due to a convolution of features arising from the 2D peaks,  $\sim 23.5\%$   $c$ -axis compression occurred at the 46-GPa transformation stress. Thus, the PG crystallites exhibited  $\sim 30\%$  more compression along the  $c$  axis than the HOPG crystallites at their respective transformation stresses.

### 2. Crystal structures and lattice parameters above phase transformation stresses

Through a detailed analysis involving determination of the lattice parameters and evaluation of the expected 2D XRD pattern [41], the diffraction data at 50 GPa show that

ZYH-grade HOPG transforms to hexagonal diamond. The diffraction pattern in Fig. 3(f) exhibits a triplet of prominent peaks with lattice spacings between 1.8 and 2.2 Å, characteristic of hexagonal diamond [5]. Cubic diamond has only a single lattice spacing between 1.8 and 2.2 Å and is, therefore, inconsistent with these results. Other proposed high-pressure carbon allotropes have more peaks between 1.8 and 2.2 Å or additional peaks at larger  $d$  spacings [26] and are, therefore, also incompatible with the observed diffraction patterns.

Past recovery experiments reporting the hexagonal diamond (HD) crystal structure relied on broad overlapping XRD peaks [5,9,12,61] which were subsequently reanalyzed

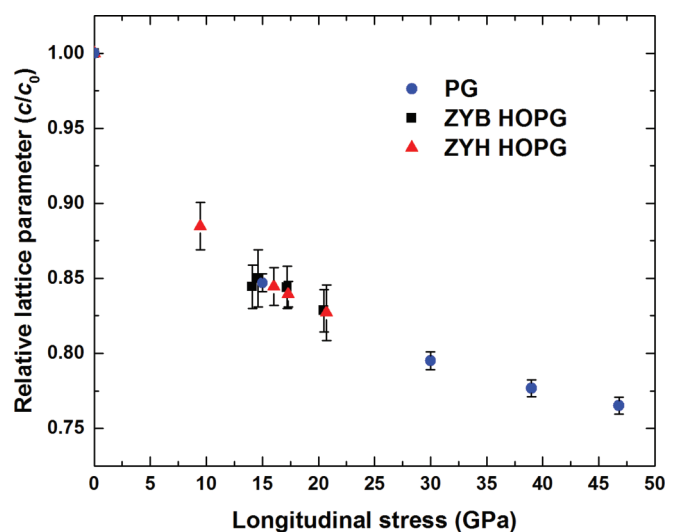


FIG. 5. Relative  $c$ -axis lattice parameters for shock-compressed HOPG and PG. The larger lattice parameter uncertainties for HOPG are due to the fact that none of the observed HOPG peaks directly provide the  $c$ -lattice parameter, whereas the (002) and (004) peaks directly provide the  $c$ -lattice parameter for PG.

and attributed to crystal structures comprising hexagonal and cubic diamond stacking [18,62]. However, the experimental configuration and materials used in this work (and the past work on ZYB-grade HOPG) [33] overcome the past limitations. Specifically, the highly textured nature of the high-pressure phase formed during the shock compression of HOPG along the  $c$  axis results in spatially isolated XRD spots allowing the lattice plane spacings to be determined from nonoverlapping peaks. Additionally, the lattice plane normals corresponding to the observed XRD spots have relative angles fully consistent with the HD crystal structure as verified by the excellent match between the simulated diffraction spots using the fiber textured HD crystal structure with  $(100)_{\text{HD}}|| (001)_{\text{HG}}$  and the observed diffraction spots (see Fig. S5) [41]. These findings conclusively show that ZYH-grade HOPG transforms to HD during plane wave shock compression to  $\sim 50$  GPa along the average  $c$  axis.

Overall, the ZYH-grade HOPG lattice-level shock response was the same at  $\sim 50$  GPa as previously reported for ZYB-grade HOPG [33]. The phase (HD), lattice parameters (reported in Table I), HD orientation, approximate mosaic spread ( $\sim 5^\circ$ ), and additional lattice strain ( $\sim 1.5\%$ ) of the high-pressure structure along the shock loading direction are all consistent with results previously reported for ZYB-grade HOPG. These findings demonstrate that the starting HOPG mosaic spread differences of a few degrees make no noticeable difference to the high-pressure phase arising from well-aligned hexagonal graphite crystallites.

Unlike HOPG, the PG examined here transforms to cubic diamond instead of hexagonal diamond. XRD simulations, broadened due to the small crystallite size, assuming diffraction from a single lattice plane provide the best overall match (Fig. S3) [41] to the bright observed upper and lower diffraction peaks shown in Fig. 3(h). An average lattice spacing of  $2.049 \pm 0.010$  Å with an average estimated crystallite size of  $\sim 47 \pm 15$  Å (using the Scherrer equation) [59] was determined from experiments 15–18. This diffraction peak was ascribed to the cubic diamond (CD) (111) peak because the lattice spacing is close to that expected for the CD (111) peak (2.034 Å)—assuming isotropic compression and an expected density of  $3.647$  g/cm<sup>3</sup> at 60 GPa based on the PG Hugoniot data [7,63]. The slightly larger observed CD (111) lattice spacing may arise from effects due to material strength and anisotropic lattice strain since the CD (111) planes resulting in the 2.049-Å lattice spacing are approximately parallel to the loading direction [41]. The lattice spacings determined from the very dim side peaks were consistent with the bright upper and lower peaks but were not used for determining the average CD lattice parameter reported in Table I, because of the low signal to noise ratio. Within experimental uncertainty, the CD density determined from the XRD-determined lattice parameters is consistent with previous Hugoniot data [7,63] and with the previous data for laser-shocked PG at 60 GPa [32].

Since diffraction from only one scattering angle was detected in our PG experiments, most other high-pressure carbon phases were ruled out. This is because most other proposed crystal structures should have more than one prominent diffraction peak [26] in the detector field of view. Due to the large mosaic spread of PG, the possibility of overlapping peaks from other proposed high-pressure crystal structures

was also considered. Performing fits to experiment 16 data using powder diffraction simulations of HD, BCT-carbon [64], and Z-carbon [24] (which have main peaks in the 2.03–2.15 Å range) gave densities 9%–11% higher than the densities obtained from continuum (or Hugoniot) measurements (see Fig. S4) [41]. Therefore, these other phases are also incompatible with our results.

Although we ascribe the observed diffraction to the CD (111) peak, due to the broad nature of the peak, very small amounts of stacking faults or local HD stacking order, as discussed by Salzmann *et al.* [62], cannot be ruled out. Considering the large mosaic spread of the high-pressure phase, diffraction from many lattice planes in the cubic diamond {111} family of lattice planes is expected to give a nearly complete diffraction ring. Thus, the observed diffracted intensity (with bright upper and lower bands) is wholly consistent with the CD high-pressure phase. However, diffraction from “amorphous diamond” would also result in a broad, smooth diffraction ring, likely broader than our observed diffraction peak [65]. Because amorphous diamond is expected to scatter at a similar angle to the (111) CD XRD peak [65], we cannot entirely rule out a small fraction of amorphous diamond coexisting with the cubic diamond in the peak shocked state. The possible amorphous phase was not quantified or considered further.

### C. Discussion

The experimental results presented here provide insights into the shock-induced formation conditions of cubic and hexagonal diamond that were not well understood in previous studies [4,7,32]. For shock loading along the average  $c$  axis below the phase transformation stress of ZYB-grade and ZYH-grade HOPG samples, the hexagonal graphite crystallites are compressed, mainly along the  $c$  axis, until, at the  $\sim 22$ -GPa transformation stress [7], the  $c$ -axis compression is  $\sim 17.5\%$ . After this  $c$ -axis compression, a concerted shifting and buckling of the graphene layers [14,15,66] can explain the formation of the observed hexagonal diamond high-pressure phase with  $(100)_{\text{HD}}|| (001)_{\text{HG}}$  for both the ZYB-grade HOPG as previously reported [33] and for the less ordered ZYH-grade HOPG as described here. The hexagonal diamond orientation we observe during shock compression has also been observed in quasistatic compression experiments [5,9,11] and is consistent with the proposed mechanism from epitaxial arguments [66] and some atomistic simulations [14,15]. The available displacive mechanism along with a lower-energy pathway for the transformation from hexagonal graphite to hexagonal diamond [67] would support its formation, despite the fact that theoretical studies suggest cubic diamond is the stable phase [14,68,69].

Mechanistically, the formation of cubic diamond from shock-compressed as-deposited pyrolytic graphite is very different from the formation of hexagonal diamond from shock-compressed highly oriented pyrolytic graphite. Despite similar  $c$ -axis graphite compression curves (see Fig. 5), the turbostratic nature of the as-deposited pyrolytic graphite crystallites and/or the large mosaic spread likely inhibits the concerted transformation to hexagonal diamond that is observed in highly oriented pyrolytic graphite. Lack of an available

concerted mechanism probably causes the additional  $\sim 30\%$  crystallite  $c$ -axis compression, relative to HOPG, observed at the PG phase transformation stress. The XRD data in Fig. 5 provide a structural basis for the previously reported higher transformation stress and additional density compression in the Hugoniot data for shock-compressed PG samples relative to HOPG [7,63,70].

Since PG is at a much higher stress and experiences more compression than HOPG at the transformation, PG is expected to be at a higher temperature [70] than HOPG [31] at the onset of the transformation. These higher temperatures likely facilitate nucleation of the more thermodynamically stable cubic diamond phase. Although simulations by Khaliullin and coauthors [15] are not for shock compression conditions and do not start with the turbostratic carbon crystal structure in the graphite, a similar barrierless nucleation mechanism initiated by the formation of a few interlayer bonds may be possible at the high stresses achieved in these experiments. The small observed cubic diamond crystallites in this work suggest that only small locally ordered regions may be nucleated at the temperatures and compressions achieved near 60 GPa. At higher stresses (and, hence, higher temperatures), Kraus *et al.* report that larger cubic diamond crystallites form based on a smaller CD (111) peak width [32]. This observation suggests that increased temperature facilitates enhanced grain growth.

Both the crystallite structures and mosaic spreads are very different between the highly oriented pyrolytic graphite and as-deposited pyrolytic graphite starting materials. The mosaic spread of a sample affects the loading direction with respect to an average crystallite within the sample. One wave profile study [71] directly examined the effect of loading direction on the transformation stress and reported that for hexagonal graphite samples shocked  $45^\circ$  from and perpendicular to the average  $c$  axis, the transformation stress remained well defined and only increased by 5%–10% relative to loading along the  $c$  axis. Based on this result [71], the large mosaic spread of PG relative to the mosaic spreads of the two HOPG types cannot solely account for the more than double transformation stress (46 GPa) of PG relative to HOPG (22 GPa) [7]. Quasistatic compression studies have reported a lack of transformation in materials comprising turbostratic carbon until the stress is over 40 GPa [72–74], whereas similar work on hexagonal graphite starting materials reported transformation stresses between 15 GPa [75] and 23 GPa [76]. These past studies [71–76], together with the findings of this work, suggest that differences in the graphite crystallite structures (hexagonal vs turbostratic) most likely govern the formation of the high-pressure phase (hexagonal diamond vs cubic diamond) rather than differences in the mosaic spread.

The understanding gained from the present work— involving plate impact shock experiments for the three graphite types—helps to reconcile the different diamond crystal structures reported previously for shocked PG [32] and ZYB-grade HOPG [33]. The diffraction line profile for ambient (unshocked) PG in Ref. [32] shows only the (002) hexagonal graphite peak and a (10) peak with a broad tail (characteristic of turbostratic carbon) [56]. The prominent (101) hexagonal graphite diffraction peak was not visible in the published diffraction data despite the detector likely having sufficient area coverage to capture diffraction from

the (101) peak—assuming the mosaic spread specified in that work [32]. Because of the diffraction features described above and because commercially available PG generally comprises highly turbostratic crystallites [77], the PG examined in Ref. [32] was likely also highly turbostratic. Therefore, the previously reported transformation [32] of a disordered PG crystal structure to CD at  $\sim 60$  GPa in laser-shock experiments is consistent with the PG results reported here for plate impact experiments.

In contrast, based on the understanding of the transformations of hexagonal graphite to hexagonal diamond and turbostratic carbon to cubic diamond presented here, the reported hexagonal diamond formation in laser-shocked PG samples above 170 GPa [32] needs reconsideration. Disorder in the starting turbostratic carbon PG crystal structure would tend to inhibit the concerted transformation pathway, discussed above for hexagonal graphite to hexagonal diamond. Furthermore, due to the lack of additional hexagonal diamond diffraction peaks, the reported diffraction doublet in Ref. [32], ascribed to the hexagonal diamond crystal structure, may instead be explained through a stacking disordered cubic diamond crystal structure [62] (see Fig. S8) [41], or through cubic diamond domains under different strains as suggested by Murri and coauthors [20]. The larger reported cubic diamond crystallites at higher stresses [32] could allow diffraction features from stacking faults and twins, obscured by size broadening effects at lower stresses, to become visible in the diffraction patterns at higher stresses. This could explain the two diffraction peaks occurring near the same location only at the highest stresses [32]. The two observable diffraction peaks suggest that the high-pressure crystal structure contains some hexagonally stacked layers [62], as would result from stacking faults or twins in the cubic diamond crystal structure. However, the formation of nearly pure hexagonal diamond seems improbable as cubic diamond is the thermodynamically more stable high-pressure phase [14,68,69]. Furthermore, the reported discontinuity in density vs shock stress [32] vanishes if the observed peak indexed as  $(002)_{\text{HD}}$  is, instead, indexed as  $(111)_{\text{CD}}$ . To definitively establish the high-pressure structure achieved in shock-compressed PG at  $\sim 200$  GPa, additional well-designed experiments are needed.

The insights gained from this study can guide future molecular dynamics simulations to compare the shock responses of hexagonal graphite and turbostratic carbon. Such simulations are important, since, to our knowledge, shock wave simulations to date have not considered turbostratic carbon as the starting material. By better understanding the idealized shock compression of turbostratic carbon along the  $c$  axis, a deeper understanding of the transformation mechanisms in individual crystallites may be gained. If successful, such results may help to disentangle the effects of crystallite size, mosaic spread, and other material parameters from the effects of crystal structure on the shock-induced graphite to diamond phase transformation.

## V. SUMMARY

To better understand the real-time formation of cubic and hexagonal diamond during shock compression of graphite and to reconcile past disparate results, *in situ* XRD measurements

were obtained during plate impact shock experiments on three graphite types. A range of crystal structures and microstructures were examined by conducting experiments on ZYB- and ZYH-grade highly oriented pyrolytic graphite and on as-deposited pyrolytic graphite. The results of this work have provided additional insights into the shock-induced graphite to diamond transformation and have reconciled past disparate findings. The main findings of this work are summarized below:

(1) Upon plate impact shock compression to  $\sim 60$  GPa, as-deposited pyrolytic graphite transforms to cubic diamond, the same structure reported in earlier laser-shock experiments on as-deposited pyrolytic graphite at  $\sim 60$  GPa [32]. Although numerous differences exist between plate impact and laser-shock experiments, this finding suggests that different shock driver systems have a smaller role than the starting graphite crystallite structure in governing the specific high-pressure diamond phase achieved at similar stresses.

(2) Upon shock compression along the average  $c$  axis to  $\sim 50$  GPa, ZYH-grade highly oriented pyrolytic graphite transforms to hexagonal diamond, with the same orientation as observed in an earlier study on the more ordered ZYB-grade highly oriented pyrolytic graphite [33]. This result definitively establishes that differences in mosaic spread have no noticeable effect on the shock response of highly oriented pyrolytic graphite above the phase transformation stress.

(3) Below the transformation, compression occurs mainly along the crystallite  $c$  axes. Although both highly oriented pyrolytic graphite grades have comparable lattice parameters just below their  $\sim 22$ -GPa phase transformation stresses, as-deposited pyrolytic graphite experiences  $\sim 30\%$  more  $c$ -axis compression at its  $\sim 46$ -GPa transformation stress. We note that the present XRD experiments on highly oriented pyrolytic graphite provided simultaneous determination of the  $a$ - and  $c$ -lattice parameters for hexagonal graphite during shock compression.

(4) Through careful characterization of the graphite samples used in this work, it was established that the starting crystal structures of the highly oriented pyrolytic graphite and as-deposited pyrolytic graphite samples examined in this study are different—both highly oriented pyrolytic graphite types comprise hexagonal graphite crystallites whereas as-deposited pyrolytic graphite comprises much more disordered, turbostratic carbon crystallites. Although the different crystal structures were not emphasized in past *in situ* XRD shock compression studies [32,33], this work demonstrates that the starting crystal structures (rather than mosaic spread) likely govern the high-pressure phase achieved upon shock compression and can explain why both cubic diamond [32] and hexagonal diamond [33] were previously observed at similar shock stresses in shocked graphite.

## ACKNOWLEDGMENTS

Dr. Pritha Renganathan, Dr. Yoshi Toyoda, and the Dynamic Compression Sector staff members (Paulo Rigg, Drew Rickerson, Robert Zill, Brendan Williams, Jeffrey Klug, Yuelin Li, Nicholas Weir, Nicholas Sinclair, and Adam Schuman) are thanked for their assistance with the plate impact experiments, x-ray beam setup, and x-ray flux characterization. Dr. J. M. Winey is thanked for useful discussions. This publication is based on work supported by the DOE/NNSA under Award No. DE-NA0002007. This publication is also based on work performed at the Dynamic Compression Sector, which is operated by Washington State University under DOE/NNSA Award No. DE-NA0002442. This research used resources of the Advanced Photon Source, a DOE Office of Science User Facility operated for the DOE Office of Science by Argonne National Laboratory under Contract No. DE-AC02-06CH11357.

- 
- [1] P. S. DeCarli and J. C. Jamieson, *Science* **133**, 1821 (1961).  
 [2] F. P. Bundy, *J. Chem. Phys.* **38**, 631 (1963).  
 [3] C. Frondel and U. B. Marvin, *Nature* **214**, 587 (1967).  
 [4] D. J. Erskine and W. J. Nellis, *Nature* **349**, 317 (1991).  
 [5] T. Yagi, W. Utsumi, M. A. Yamakata, T. Kikegawa, and O. Shimomura, *Phys. Rev. B* **46**, 6031 (1992).  
 [6] F. P. Bundy, W. A. Bassett, M. S. Weathers, R. J. Hemley, H. K. Mao, and A. F. Goncharov, *Carbon* **34**, 141 (1996).  
 [7] T. J. Volz and Y. M. Gupta, *J. Appl. Phys.* **125**, 245902 (2019).  
 [8] W. Baek, S. A. Gromilov, A. V. Kuklin, E. A. Kovaleva, A. S. Fedorov, A. S. Sukhikh, M. Hanfland, V. A. Pomogaev, I. A. Melchakova, P. V. Avramov, and K. V. Yuzenko, *Nano Lett.* **19**, 1570 (2019).  
 [9] A. Yoshiasa, Y. Murai, O. Ohtaka, and T. Katsura, *Jpn. J. Appl. Phys.* **42**, 1694 (2003).  
 [10] C. Le Guillou, F. Brunet, T. Irifune, H. Ohfujii, and J. N. Rouzaud, *Carbon* **45**, 636 (2007).  
 [11] F. P. Bundy and J. S. Kasper, *J. Chem. Phys.* **46**, 3437 (1967).  
 [12] W. Utsumi, M. Yamakata, T. Yagi, and O. Shimomura, in *Proceedings of the 15th AIRAPT Conference*, AIP Conf. Proc. No. 309 (AIP, Melville, NY, 1994), p. 535.  
 [13] S. Fahy, S. G. Louie, and M. L. Cohen, *Phys. Rev. B* **34**, 1191 (1986).  
 [14] Y. Tateyama, T. Ogitsu, K. Kusakabe, and S. Tsuneyuki, *Phys. Rev. B* **54**, 14994 (1996).  
 [15] R. Z. Khaliullin, H. Eshet, T. D. Kühne, J. Behler, and M. Parrinello, *Nat. Mater.* **10**, 693 (2011).  
 [16] Z. Pan, H. Sun, Y. Zhang, and C. Chen, *Phys. Rev. Lett.* **102**, 055503 (2009).  
 [17] L. Qingkun, S. Yi, L. Zhiyuan, and Z. Yu, *Scr. Mater.* **65**, 229 (2011).  
 [18] P. Németh, L. A. J. Garvie, T. Aoki, N. Dubrovinskaia, L. Dubrovinsky, and P. R. Buseck, *Nat. Commun.* **5**, 5447 (2014).  
 [19] A. P. Jones, P. F. McMillan, C. G. Salzmann, M. Alvaro, F. Nestola, M. Prencipe, D. Dobson, R. Hazael, and M. Moore, *Lithos* **265**, 214 (2016).  
 [20] M. Murri, R. L. Smith, K. McColl, M. Hart, M. Alvaro, A. P. Jones, P. Németh, C. G. Salzmann, F. Corà, M. C. Domeneghetti, F. Nestola, N. V. Sobolev, S. A. Vishnevsky, A. M. Logvinova, and P. F. McMillan, *Sci. Rep.* **9**, 10334 (2019).  
 [21] Q. Li, Y. Ma, A. R. Oganov, H. Wang, H. Wang, Y. Xu, T. Cui, H. K. Mao, and G. Zou, *Phys. Rev. Lett.* **102**, 175506 (2009).

- [22] K. Umemoto, R. M. Wentzcovitch, S. Saito, and T. Miyake, *Phys. Rev. Lett.* **104**, 125504 (2010).
- [23] J. T. Wang, C. Chen, and Y. Kawazoe, *Phys. Rev. Lett.* **106**, 075501 (2011).
- [24] M. Amsler, J. A. Flores-Livas, L. Lehtovaara, F. Balima, S. A. Ghasemi, D. Machon, S. Pailhès, A. Willand, D. Caliste, S. Botti, A. San Miguel, S. Goedecker, and M. A. L. Marques, *Phys. Rev. Lett.* **108**, 065501 (2012).
- [25] H. Niu, X. Q. Chen, S. Wang, D. Li, W. L. Mao, and Y. Li, *Phys. Rev. Lett.* **108**, 135501 (2012).
- [26] Y. Wang, J. E. Panzik, B. Kiefer, and K. K. M. Lee, *Sci. Rep.* **2**, 520 (2012).
- [27] M. E. Lipschutz and E. Anders, *Science* **134**, 2095 (1961).
- [28] M. E. Lipschutz, *Science* **143**, 1431 (1964).
- [29] R. S. Clarke, Jr., D. E. Appleman, and D. R. Ross, *Nature* **291**, 396 (1981).
- [30] D. J. Kennett, J. P. Kennett, A. West, G. J. West, T. E. Bunch, B. J. Culleton, J. M. Erlandson, S. S. Que Hee, J. R. Johnson, C. Mercer, F. Shen, M. Sellers, T. W. Stafford, A. Stich, J. C. Weaver, J. H. Wittke, and W. S. Wolbach, *Proc. Natl. Acad. Sci. USA* **106**, 12623 (2009).
- [31] D. J. Erskine and W. J. Nellis, *J. Appl. Phys.* **71**, 4882 (1992).
- [32] D. Kraus, A. Rvasio, M. Gauthier, D. O. Gericke, J. Vorberger, S. Frydrych, J. Helfrich, L. B. Fletcher, G. Schaumann, B. Nagler, B. Barbrel, B. Bachmann, E. J. Gamboa, S. Göde, E. Granados, G. Gregori, H. J. Lee, P. Neumayer, W. Schumaker, T. Döppner *et al.*, *Nat. Commun.* **7**, 10970 (2016).
- [33] S. J. Turneaure, S. M. Sharma, T. J. Volz, J. M. Winey, and Y. M. Gupta, *Sci. Adv.* **3**, eaao3561 (2017).
- [34] S. Scandolo, M. Bernasconi, G. L. Chiarotti, P. Focher, and E. Tosatti, *Phys. Rev. Lett.* **74**, 4015 (1995).
- [35] C. J. Mundy, A. Curioni, N. Goldman, I.-F. W. Kuo, E. J. Reed, L. E. Fried, and M. Ianuzzi, *J. Chem. Phys.* **128**, 184701 (2008).
- [36] N. Pineau, *J. Phys. Chem. C* **117**, 12778 (2013).
- [37] M. P. Kroonblawd and N. Goldman, *Phys. Rev. B* **97**, 184106 (2018).
- [38] L. M. Barker and R. E. Hollenbach, *J. Appl. Phys.* **43**, 4669 (1972).
- [39] W. F. Hemsing, *Rev. Sci. Instrum.* **50**, 73 (1979).
- [40] O. T. Strand, D. R. Goosman, C. Martinez, T. L. Whitworth, and W. W. Kuhlow, *Rev. Sci. Instrum.* **77**, 083108 (2006).
- [41] See Supplemental Material at <http://link.aps.org/supplemental/10.1103/PhysRevB.101.224109> for additional experimental details, analysis methods, and results; also see Refs. [42–46].
- [42] R. G. McQueen, S. P. Marsh, and J. N. Fritz, *J. Geophys. Res.* **72**, 4999 (1967).
- [43] *LASL Shock Hugoniot Data*, edited by S. P. Marsh (University of California Press, Berkeley, CA, 1980).
- [44] J. E. Field, *Rep. Prog. Phys.* **75**, 126505 (2012).
- [45] P. A. Rigg, M. D. Knudson, R. J. Scharff, and R. S. Hixson, *J. Appl. Phys.* **116**, 033515 (2014).
- [46] J. M. Winey, A. Hmiel, and Y. M. Gupta, *J. Phys. Chem. Solids* **93**, 118 (2016).
- [47] H. J. McSkimin and P. Andreatch, *J. Acoust. Soc. Am.* **34**, 609 (1962).
- [48] O. L. Blakslee, D. G. Proctor, E. J. Seldin, G. B. Spence, and T. Weng, *J. Appl. Phys.* **41**, 3373 (1970).
- [49] M. Lucas, J. M. Winey, and Y. M. Gupta, *J. Appl. Phys.* **114**, 093515 (2013).
- [50] A. W. Moore, in *Chemistry and Physics of Carbon: Vol. 11*, edited by P. L. Walker, Jr. and P. A. Thrower (Dekker, New York, 1973), pp. 69–187.
- [51] J. Maire and J. Mering, in *Chemistry and Physics of Carbon: Vol. 6*, edited by P. L. Walker, Jr. (Marcel Dekker, New York, 1970), pp. 125–190.
- [52] W. Ruland, in *Chemistry and Physics of Carbon: Vol. 4*, edited by P. L. Walker, Jr. (Dekker, New York, 1968), pp. 1–84.
- [53] G. E. Bacon, *Acta Crystallogr.* **4**, 558 (1951).
- [54] O. J. Guentert and S. Cvikevich, in *Proceedings of the Fifth Conference on Carbon* (Pergamon Press, Oxford, 1961), pp. 473–484.
- [55] R. E. Franklin, *Acta Crystallogr.* **4**, 253 (1951).
- [56] B. E. Warren, *Phys. Rev.* **59**, 693 (1941).
- [57] C. L. Melcher and J. S. Schweitzer, *IEEE Trans. Nucl. Sci.* **39**, 502 (1992).
- [58] A. P. Hammersley, S. O. Svensson, M. Hanfland, A. N. Fitch, and D. Hausermann, *High Pressure Res.* **14**, 235 (1996).
- [59] B. E. Warren, *X-Ray Diffraction* (Addison-Wesley Publishing Company, Reading, MA, 1969).
- [60] Q. Johnson, A. C. Mitchell, and L. Evans, *Appl. Phys. Lett.* **21**, 29 (1972).
- [61] R. E. Hanneman, H. M. Strong, and F. P. Bundy, *Science* **155**, 995 (1967).
- [62] C. G. Salzmann, B. J. Murray, and J. J. Shephard, *Diamond Relat. Mater.* **59**, 69 (2015).
- [63] W. H. Gust, *Phys. Rev. B* **22**, 4744 (1980).
- [64] X.-F. Zhou, G.-R. Qian, X. Dong, L. Zhang, Y. Tian, and H.-T. Wang, *Phys. Rev. B* **82**, 134126 (2010).
- [65] Z. Zeng, L. Yang, Q. Zeng, H. Lou, H. Sheng, J. Wen, D. J. Miller, Y. Meng, W. Yang, W. L. Mao, and H. K. Mao, *Nat. Commun.* **8**, 322 (2017).
- [66] K. Lonsdale, *Am. Mineral.* **56**, 333 (1971).
- [67] Y. P. Xie, X. J. Zhang, and Z. P. Liu, *J. Am. Chem. Soc.* **139**, 2545 (2017).
- [68] S. Fahy and S. G. Louie, *Phys. Rev. B* **36**, 3373 (1987).
- [69] B. R. Wu and J.-A. Xu, *Phys. Rev. B* **57**, 13355 (1998).
- [70] N. L. Coleburn, *J. Chem. Phys.* **40**, 71 (1964).
- [71] G. I. Kanel, G. S. Bezruchko, A. S. Savinykh, S. V. Razorenov, V. V. Milyavskii, and K. V. Khishchenko, *High Temp.* **48**, 806 (2010).
- [72] G. A. Samara and H. G. Drickamer, *J. Chem. Phys.* **37**, 471 (1962).
- [73] A. F. Goncharov, *Sov. Phys. JETP* **71**, 1025 (1990).
- [74] A. Nakayama, S. Iijima, Y. Koga, K. Shimizu, K. Hirahara, and F. Kokai, *Appl. Phys. Lett.* **84**, 5112 (2004).
- [75] R. B. Aust and H. G. Drickamer, *Science* **140**, 817 (1963).
- [76] A. F. Goncharov, *JETP Lett.* **51**, 418 (1990).
- [77] W. H. Smith and D. H. Leeds, in *Modern Materials*, edited by B. W. Gosser (Academic Press, Inc., New York, 1970), pp. 139–221.